Energy Advances

ROYAL SOCIETY OF CHEMISTRY

PAPER

View Article Online
View Journal | View Issue

Cite this: *Energy Adv.*, 2025, 4, 1032

Poly(ethyleneimine) modified TiO_2 nanorods for adsorptive recovery of lithium from a battery cathode and brine solution†

K. Krishna Priyanka,[a] M. Christina Nilavu,[a] Arunraj Balasubramanian,[b] Himanshu Aggarwal *[a] and N. Rajesh *[a]

Received 4th April 2025,
Accepted 2nd June 2025

DOI: 10.1039/d5ya00092k

rsc.li/energy-advances

Lithium, often referred to as 'white gold,' is a vital element in modern technology, and its applications are found in various fields, including Li-ion batteries (LIBs). Being explored for countless technological applications, lithium recovery from spent batteries is a significant concern. In this study, we report a titanium nanorod-based adsorbent modified with PEI for the adsorptive removal of lithium from various sources. The hydrothermally synthesized adsorbent was mesoporous, with a specific surface area of 45.8 m^2 g^{-1}. The characteristics of the adsorbent material were corroborated using multiple analytical techniques such as BET-N_2 isotherm analysis, XPS, PXRD, TGA, FESEM-EDS, FTIR, and DLS. The maximum adsorption capacity of the material under optimized conditions was 2.76 mg g^{-1}. The adsorption process was endothermic and feasible, fitting well with the Langmuir isotherm following pseudo-first-order kinetics. The spent adsorbent was recovered and exhibited a regeneration capacity of up to 4 cycles. Furthermore, desorbed lithium was successfully converted into Li_2O, contributing to a circular economy.

1. Introduction

Lithium is the 33rd most prevalent element in the Earth's crust, with its concentration ranging from 20 ppm to 70 ppm. It is among the lightest and least dense alkali metals and is also highly reactive. Lithium is considered a critical element called the "new white gold."[1] Since its discovery, it has become an indispensable material owing to its various applications, with the majority being in the energy industry, which includes lithium batteries.[2,3] Lithium batteries are widely used in portable electronic devices due to the unique properties of the Li-ion, such as high energy density, compact size, highest specific heat capacity, outstanding electrochemical features, wide working temperature, long lifespan, *etc.*, making them an attractive choice and superior to any other energy storage devices.[4,5] Lithium also finds applications in various other fields, including ceramics, lubricating agent, pharmaceuticals, as an antipsychotic drug, *etc.*[6,7] One of the most common areas where lithium has been widely utilized is Li-ion batteries (LIBs). With the steadfast demand for LIBs and the transition towards cleaner and more sustainable energy systems, LIBs have become the basis of this change, necessitating an in-depth exploration of various lithium recovery methods more than ever. Lithium recovery from various sources was investigated, including seawater,[8] salt lakes,[9] brine solutions,[10] *etc.* However, due to a very low concentration (0.17 ppm),[11] they may not satisfy the growing demand for lithium. In recent years, the increased growth towards the development of cleaner energy has led to the introduction of LIBs in the global market, with their accelerated production rate due to their excellent benefits over other technologies. Various techniques have been established for recovery, such as co-precipitation,[12] chromatography,[13] liquid extraction[14] and adsorption,[15–17] membrane-based technologies,[18] use of microorganisms,[19] solvent extraction, *etc.* Conventional techniques like pyrometallurgy and hydrometallurgy[20,21] are undoubtedly the direct methods for the recycling process and can be considered simple procedures. However, these techniques have certain disadvantages, which include the production of secondary waste and harmful gases, the use of toxic solvents and their improper discharge, sophisticated requirements, high-cost material and technology, consumption of high energy,[22] limited recovery of other valuable elements apart from lithium, *etc.* Consequently, there are

[a] *Department of Chemistry, Birla Institute of Technology and Science, Hyderabad Campus, Jawahar Nagar, Kapra Mandal, Medchal District, Pilani, Telangana, 500078, India. E-mail: nrajesh@hyderabad.bits-pilani.ac.in, himanshu.aggarwal@hyderabad.bits-pilani.ac.in*

[b] *Maseeh Department of Civil, Architectural and Environmental Engineering, University of Texas, Austin, TX, 78712, USA*

† Electronic supplementary information (ESI) available. See DOI: https://doi.org/10.1039/d5ya00092k

numerous reports on environmental and financial issues brought about by the production and consumption of LIBs;[23] hence, proper management of spent LIBs is necessary, which would reduce environmental impacts and encourage a circular economy by reintroducing valuable end-of-life materials.[24] To find sustainable ways to recover this precious metal, bioleaching has been explored. However, this approach relies on specific microorganisms, is relatively slow, and has low efficiency. Additionally, harmful heavy metal ions in batteries can inhibit bacterial growth, further limiting the process's effectiveness. Adsorption has the most advantages due to its low cost, simplicity in preparing the materials with a maximum sustainable approach, high selectivity, easy tunability, and low energy consumption. Several adsorbents have been investigated for lithium adsorption, including carbon-based,[25] lithium-ion sieves, metal ion and carbon-based composites, LDHs,[26,27] spinels, *etc.* Metal ion-based adsorbents, in particular aluminium,[28] manganese, and titanium, have been less explored; one of the significant disadvantages of utilizing manganese-based adsorbents is their dissolution, which reduces their efficiency, thus affecting their reusability over cycles. Titanium-based adsorbents have received increasing interest in recent years due to their exceptional stability in an acidic environment, comparatively reduced dissolution compared to the manganese-based adsorbents, non-leaching properties, effective ion exchange characteristics, and recyclability.[29–31]

In this study, we designed a titanium nanorod and polymer composite through facile hydrothermal synthesis, after which it was mixed with the polymer in a 1 : 1 ratio, with ethanol being the reaction medium under mechanical stirring. We also investigated its lithium adsorption performance by conducting batch adsorption experiments and optimizing parameters such as dosage, pH, contact time, and initial lithium-ion concentrations. Kinetic studies were performed and applied to various models to identify the adsorption mechanism. The desorption experiments were carried out to test the efficiency and reusability of the adsorbent. The synthesized adsorbent was also utilized for the adsorption of lithium from $LiCoO_2$ and highly alkaline sodium chloride brine, followed by its desorption using 2.0 M H_3PO_4. Lithium was further converted to lithium oxide, contributing towards a circular economy.

2. Materials and methods

2.1. Materials

Titanium dioxide nanopowder, lithium chloride, and $LiCoO_2$ were obtained from Sisco Research Laboratories India. Polyethyleneimine (PEI) was obtained from Sigma Aldrich. Sodium hydroxide was obtained from SD Fine Chemicals Ltd, India. Ethanol (99% pure) was obtained from Bio Liqua Research Pvt. Ltd. Methanol (HPLC grade) was obtained from Thermo Fisher Scientific India Pvt. Ltd. Sodium chloride was obtained from Merck, and Milli-Q water was used throughout the preparation of various solutions. All the reagents and chemicals used throughout the study were of analytical grade and used without further purification. Thorin (disodium; 4-[(2-arsonophenyl)diazinyl]-3-hydroxynaphthalene-2,7-disulphonate) was obtained from Sisco Research Laboratories, India.

2.2. Preparation of the adsorbent

2.2.1. Preparation of TiO_2 nanorods. The synthetic procedure for preparing TiO_2 nanorods was according to a previously reported method.[32,33] Briefly, 1.5 g of TiO_2 nanopowder was added to 50 mL of 10.0 M NaOH and stirred over a magnetic stirrer for 1 h. After this, the mixture was sonicated for 10 min to attain a uniform dispersion, and the resulting suspension was transferred to a 100 mL Teflon-lined autoclave and heated in the oven at 150 °C for 48 h. The nanorods were filtered and washed with dilute HCl and deionized water until the pH was neutral at room temperature, and subsequently, they were dried in a vacuum oven at 80 °C for 24 h.

2.2.2. Preparation of a 1 : 1 TiO_2 nanorod modified PEI composite. 1.0 g of polyethyleneimine was weighed in a round-bottom flask to which 10 mL of ethanol was added and magnetically stirred at 50 °C until the polymer was homogenously dissolved and evenly dispersed. 1.0 g of the prepared titanium dioxide nanorods from the previous step was added to this PEI mixture and kept stirring overnight at 80 °C. The final product was dried in a vacuum oven at 80 °C and named TiO_2(NR)–PEI, as shown in Scheme 1. This was subsequently characterized and utilized for adsorption studies. In the adsorbent synthesis, the PEI ratio was varied and it was observed during the preliminary study that adsorption was most effective at a 1 : 1 TiO_2(NR):PEI ratio. When the PEI content exceeded TiO_2(NR) (ratio above 1 : 1), the characteristics of the material changed significantly and it was agglomerated, uneven and no longer in powder form. Additionally, as the polymer ratio increased beyond that of the titanium nanorods, the surface area also decreased leading to a decline in adsorption. Conversely, at lower PEI ratios, the adsorption efficiency was also lower than the 1 : 1 TiO_2(NR) to PEI ratio, making this an optimal choice for synthesizing the adsorbent.

2.3. Preparation of lithium solution and the calibration range

To prepare a stock solution of lithium (1000 mg L^{-1}), 6.14 g of lithium chloride was taken and dissolved in 1000 mL of Milli-Q water. The calibration curve was obtained by preparing a series of concentrations from 2 to 10 mg L^{-1} and quantified using ion chromatography with a distinct peak for lithium at 8.3 min retention time. An additional UV-vis spectrophotometric method was developed where thorin was used as a complexing agent for lithium, and absorbance was measured at 473 nm for the complex.

2.4. Batch adsorption studies

To perform the batch adsorption experiments, 10–100 mg L^{-1} lithium was prepared from the stock solution. Lithium solution was taken in a centrifuge tube with 0.15 g of adsorbent and kept for adsorption over a vortex shaker for 180 min at 720 rpm. Lithium concentration before and after adsorption was quantified using ion chromatography (eluent: 7.5 mmol L^{-1} tartaric

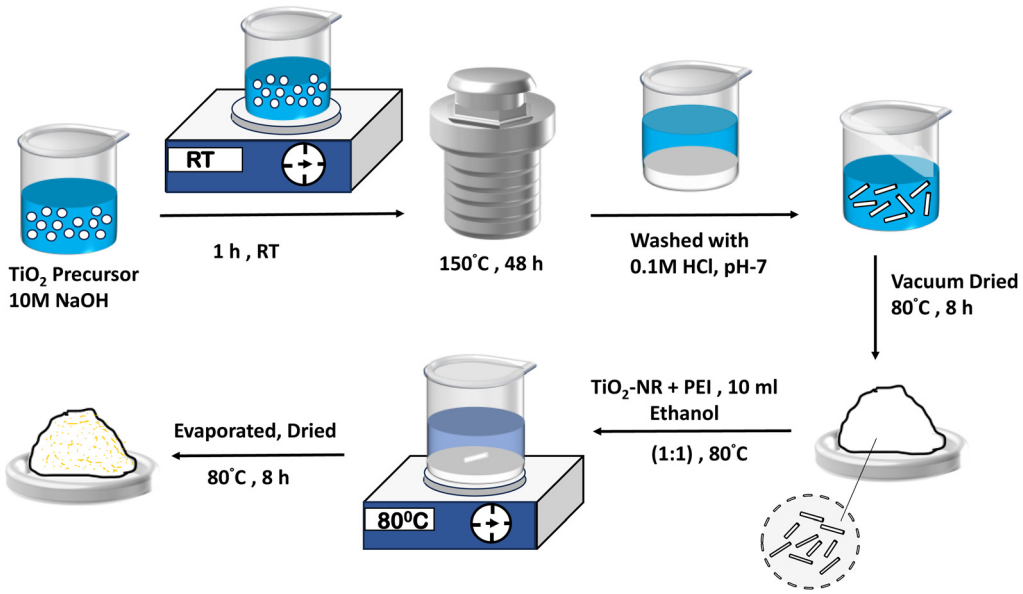

Scheme 1 Schematic representation of the preparation of the PEI-modified nanorod adsorbent.

acid and 4 mmol L^{-1} HNO_3). Dilution factors were also accounted for in all the prepared solutions. The equilibrium adsorption capacity (q_e) of the prepared adsorbent was calculated using the formula,

$$q_e = \frac{(C_0 - C_e)V}{W} \quad (1)$$

where C_0 and C_e are the initial and equilibrium concentrations of lithium, respectively. V and W represent the volume of lithium solution in (L) and the weight of the adsorbent in (g), respectively. Desorption was also performed using phosphoric acid. Fig. 1 presents the absorption spectrum of the sample solution before and after lithium adsorption and desorption.

Absorbance values at λ_{max} 473 nm were recorded to quantify lithium before and after adsorption. A decrease in absorbance confirms the decline in lithium concentration in the solution. Fig. S1 and S2, ESI† present the calibration plots obtained from UV-vis spectrophotometry and ion chromatography.

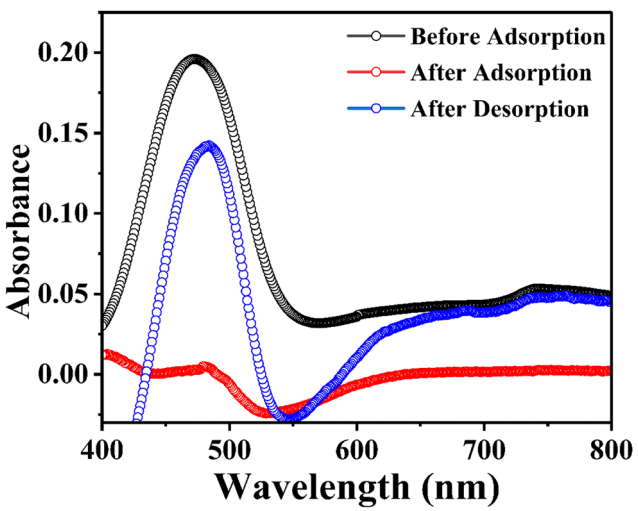

Fig. 1 Absorption spectra of lithium before adsorption, after adsorption, and desorption.

2.5. Instrumentation for analysis of lithium and adsorbent characterization

Lithium quantification was done using a Jasco-V650 spectrophotometer with 10 mm matched quartz cuvettes at 473 nm. The concentration of lithium before and after adsorption was also ascertained using ion chromatography (Metrohm 883 Basic Plus IC, Nucleosil 5SA-125/4.0 Column).

The adsorption process was performed using a Tabletop Vortex shaker (VSMP LabQuest, BOROSIL) at 700 rpm. An attenuated total reflectance (ATR) Alpha II spectrometer, with a room temperature DTGS1 detector, was used to interpret vibrational frequency shift in functional groups of the adsorbent between 500 and 4000 cm^{-1}; KBr pellets were prepared for the analysis where KBr was grounded along with the adsorbent material in the ratio 3 : 1. To analyze the surface morphology and elemental composition, SEM-EDS was obtained using an FEI Apero-LoVac scanning electron microscope with an Oxford X-Max EDS. The shift in the binding energy of the elements in the adsorbent was analyzed using X-ray photoelectron spectroscopy, which was recorded using a Thermo Scientific K-Alpha (Al-Kα monochromator) XPS instrument. The nature of the adsorbent material (crystalline/amorphous) was recorded using a Rigaku Ultima-IV X-ray diffractometer with Cu-Kα radiation (1.5405 Å) over a 2θ range of 10° to 80°. Surface area, pore volume, and pore diameter were ascertained through BET analysis using a Microtrac Bel (BELSORP mini II) BET surface analyzer. Sample pretreatment involved degassing of the sample at 100 °C for 2 h and N_2 adsorption. The particle size was measured using the DLS technique (Anton Paar).

3. Results and discussion

3.1. Characterisation of the adsorbent

3.1.1. FTIR analysis and X-ray fluorescence analysis of the adsorbent. The functional groups of the adsorbent material and their stretching frequencies were analyzed using FTIR spectra (Fig. 2). The bands in the range of 3000–3500 cm^{-1} are attributed to the stretching vibration of H_2O molecules (Fig. 2a), and the band observed at 1625 cm^{-1} is associated with the bending mode of the water molecule. Distinct peaks in the range of 400–850 cm^{-1} region correspond to the Ti–O and Ti–O–Ti skeletal frequencies. A small peak at 1396 cm^{-1} is due to the protonation of the surface Ti–OH^{2+} groups.[34] After incorporating polyethyleneimine, new peaks were observed (Fig. 2b). The broad band around 3400 cm^{-1} results from the overlap of N–H (stretch) and O–H (stretch) vibrations.[35] The peak at 2931 cm^{-1} and 2830 cm^{-1} corresponds to C–H stretch, the peak at 1471 cm^{-1} signifies C–H bending, and the peak at 1635 cm^{-1} corresponds to N–H bending.[36] The peak at 1581 cm^{-1} is assigned to the C═N stretching mode;[37] other bands at 1372 cm^{-1}, 1109 cm^{-1}, and 1049 cm^{-1} correspond to C–N bonds.[38] The intensity of the IR peaks decreased after adsorption of lithium. This reduction suggests that the adsorbed metal ion modifies the electronic environment, which leads to a decrease in the intensity of vibrational modes, potentially due to electrostatic interactions with the functional groups present on the adsorbent. As shown in (Fig. 2c), there is a notable decrease in the intensity of the peaks, especially for the amine group, accompanied by a slight shift. X-ray fluorescence (XRF) was employed to confirm the presence and percentage of titanium in the adsorbent (Fig. 2d). High-energy X-rays are directed at the sample, which leads to the expulsion of electrons from the innermost shell, the *K* shell. K_α radiation corresponds to the energy released by the electrons, which are de-excited from the *L* shell, and K_β by the electrons from the *M* shell. Since the energy gap between orbitals is different for different elements, it is used for qualitative analysis of components present in the sample. The presence of lithium, carbon, and nitrogen cannot be detected through XRF owing to their light atomic weight as their fluorescence yield is relatively low. Also, the secondary X-rays emitted by these light-weight atoms are of very low energy, which would diffuse in the surroundings before they reach the detector for detection.

3.1.2. Surface characterization of the adsorbent. The surface morphology and composition of the prepared TiO_2-NRs

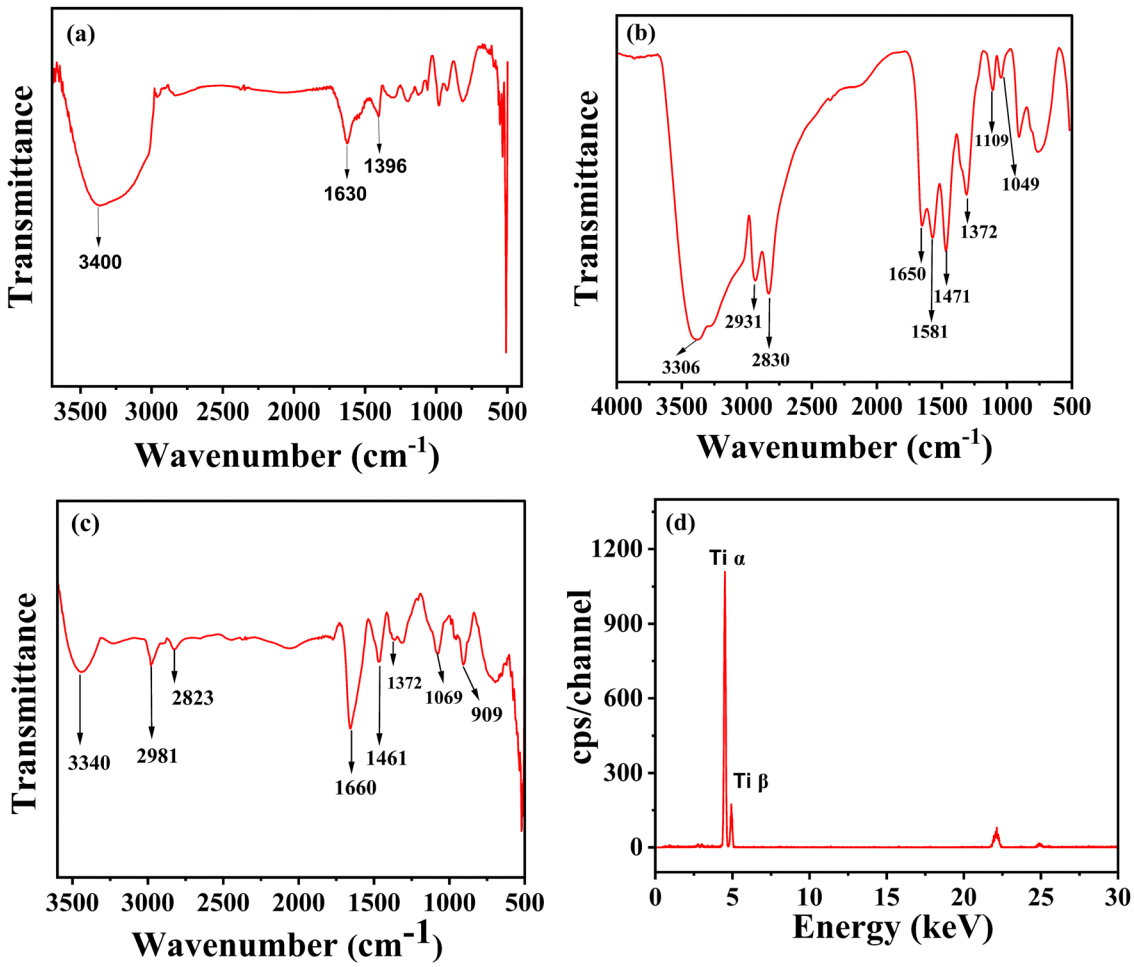

Fig. 2 FTIR spectra of (a) TiO_2-NRs, (b) TiO_2(NRs)-PEI before adsorption, (c) TiO_2(NRs)-PEI after adsorption, and (d) XRF spectrum of the TiO_2-NR adsorbent.

and TiO_2(NRs)–PEI were characterized using FESEM and EDS analysis. Prior to SEM analysis, a thin layer (10 nm) of gold film was sputtered over the sample. Scanning electron microscopic characterization shows the surface features of the samples at high resolution in the nanometer range (Fig. 3a and b). SEM images of the precursor TiO_2-NRs before and after modification with PEI reveal that the rod-like morphology of the precursor has been observed, confirming the intended structure of TiO_2-NRs.[39] It can be observed that after modifying the titanium nanorods with polyethyleneimine, there was an infinitesimal change in the morphology of the rods. However, a reticular type of accumulation has been observed, affirming a distinctive change in morphology after modifying the nanorods with the polymer. Fig. 3d depicts the SEM image of the adsorbent after 4 cycles of adsorption. It can be observed that after completing 4 cycles of adsorption, the morphology was no longer rod-like and

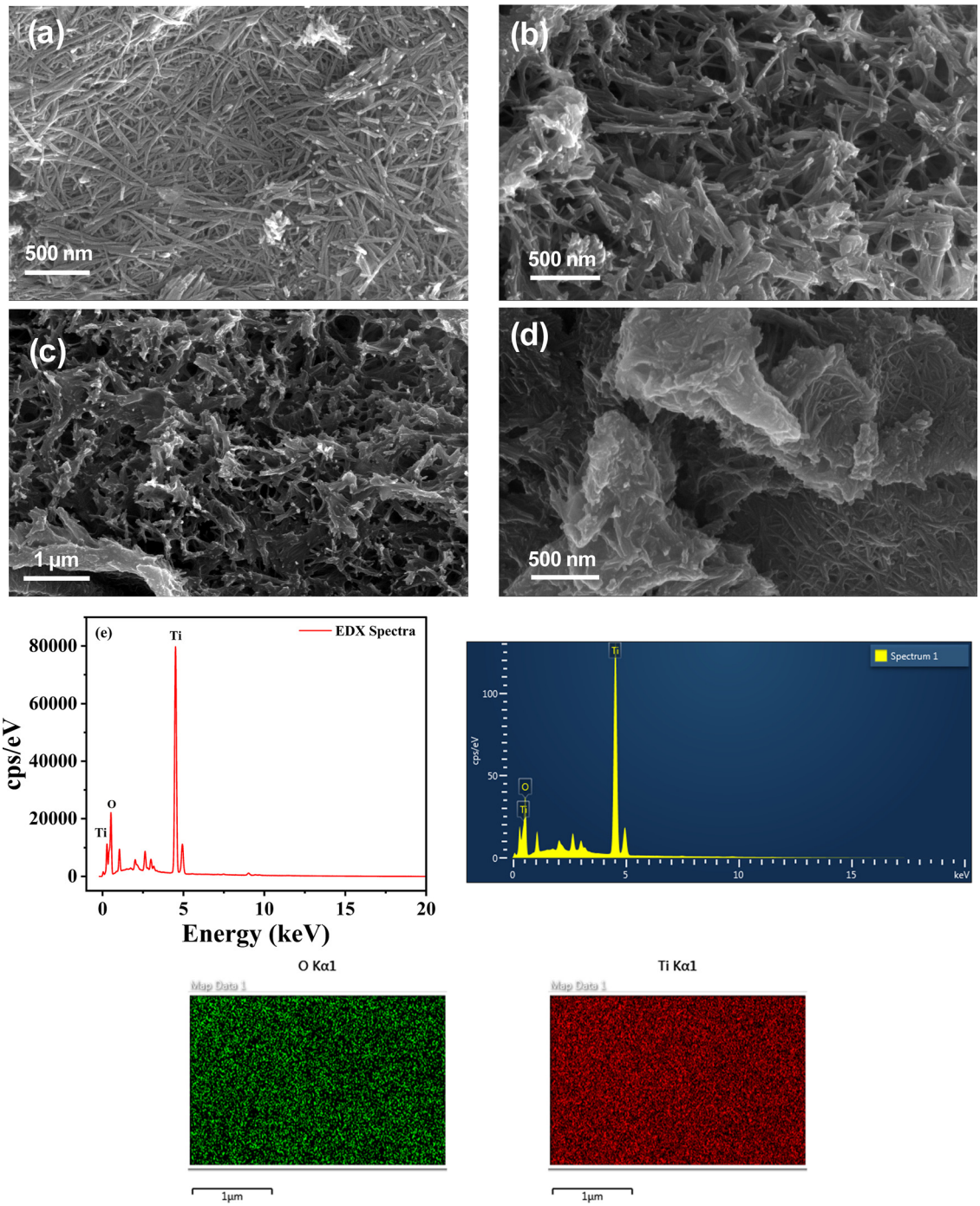

Fig. 3 SEM images of (a) TiO_2-NRs, (b) TiO_2(NRs)–PEI, (c) after adsorption, (d) after four cycles of desorption, (e) EDS spectrum of dTiO_2-NRs, (f) and (g) elemental mapping analysis of Ti and O of the adsorbent.

had agglomerated. This can be attributed to using 2.0 M H_3PO_4 in each instance for desorption, which leads to structural deformation and aggregation. EDS and mapping were performed to analyse the prepared adsorbent's elemental composition on its surface. Fig. 3e confirms the abundance of titanium along with the presence of oxygen and the elemental composition is provided in Table S5 (ESI†). Notably, the presence of lithium, after adsorption, cannot be detected as its atomic number is relatively low and hence, X-rays emitted from these light elements are of lower energy and are difficult to detect.

3.1.3. Thermogravimetric analysis of the adsorbent. TGA/DTA techniques are commonly used to assess the thermal stability of materials. TGA was performed for TiO_2-NRs and TiO_2(NRs)PEI under a nitrogen atmosphere between 10 and 800 °C. The TGA plot (Fig. 4) shows about 7% weight reduction in the TiO_2-NRs at 110 °C, which is attributed to the loss of water molecules.[40] Notably, there was no further decrease in the weight up to 800 °C, which indicates that the material is thermally stable. Three weight loss events were observed for TiO_2(NR)–PEI. Initially, a 10% weight loss at 75 °C was observed, corresponding to the loss of ethanol, which was used as the solvent. The second stage involved a weight loss of 7% between 75 °C and 270 °C, which was attributed to the loss of the organic moiety from the polymer. The third stage, a significant weight loss of about 40% between 288 °C and 382 °C, corresponds to the slow degradation of the polymer backbone and a steady plateau can be observed above 390 °C, indicating the thermal degradation of the adsorbent.[41]

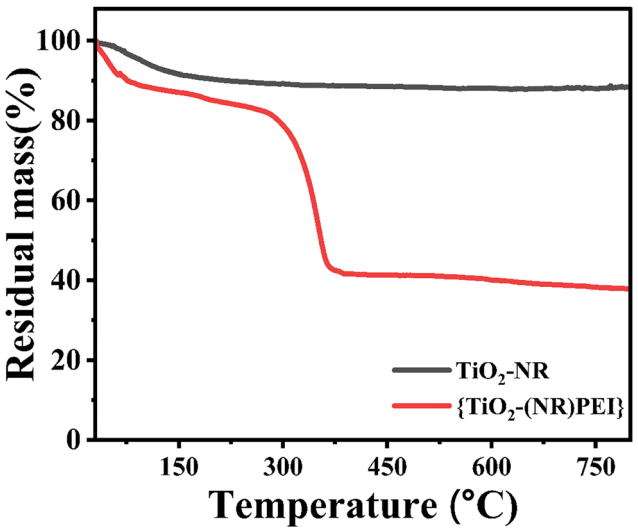

Fig. 4 Thermogravimetric analysis of the precursor TiO_2-NRs and TiO_2(NRs)–PEI.

3.1.4. Powder XRD analysis of TiO_2-NRs and TiO_2(NRs)PEI before adsorption. The X-ray diffraction pattern of TiO_2-NR shows crystalline peaks at specific 2θ values of 25.20° (101), 37.52° (004), 47.87° (200), 53.53° (105), 54.86° (211), 62.36° (204), 70.03° (220), 74.626° (215), and 75.74° (301). As depicted in Fig. 5, these peaks correspond to the earlier reported anatase phase of TiO_2 with unit cell parameters a = 3.7824 Å and c = 9.514 Å.[42] The interplanar distances calculated from these peaks are 3.52 Å, 2.39 Å, 1.89 Å, 1.71 Å, 1.67 Å, 1.48 Å, 1.34 Å, 1.27 Å, and 1.25 Å. Upon modification of prepared titanium nanorods, 2θ values were found to be 27.43° (110), 36.08° (101), 41.24° (111), 54.32° (211), 56.62° (220), 62.75° (002), 69.00° (301), and 69.80° (112). The interplanar distances for these modified peaks are 3.25 Å, 2.48 Å, 2.18 Å, 1.88 Å, 1.68 Å, 1.62 Å, 1.47 Å, 1.35 Å, and 1.34 Å. It can be observed that upon modification, the d-spacing has increased, which can be due to the modification of nanorods with polyethyleneimine, which aids in additional functional groups on the surface of the TiO_2NR, forming a composite altering the domain, thereby increasing the interplanar distance.

3.1.5. XPS analysis of the adsorbent before and after adsorption. X-ray photoelectron spectroscopy (XPS) was performed to confirm the chemical composition of the elements on the surface of the adsorbent. A plot of binding energy *vs.* intensity/counts is obtained for the quantitative analysis of the

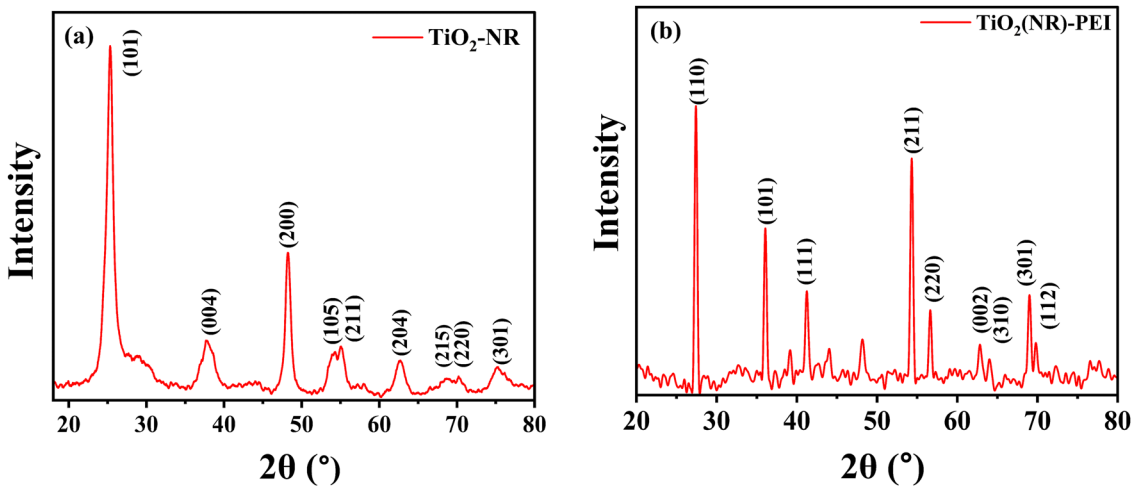

Fig. 5 Powder X-ray diffraction patterns of (a) TiO_2-NRs and (b) TiO_2(NRs)–PEI.

elements. The XPS survey spectrum was recorded from a binding energy between 100 and 1400 eV. Fig. 6a presents the survey spectrum of the adsorbent before and after adsorption. The survey spectrum confirms the presence of Ti, C, O, and N before and after adsorption. Notably, the intensity of the O 1s peak has decreased after modification with the polymer, indicating that the metal ion has coordinated with the oxygen functionalities of the titanium nanorods, and that of N 1s has decreased after adsorption, suggesting that nitrogen could have been directly involved in the adsorption of lithium. Fig. 6b illustrates the deconvoluted spectra of N 1s, where a slight increase in the binding energy of NH_2, NH, and N_3^+ from

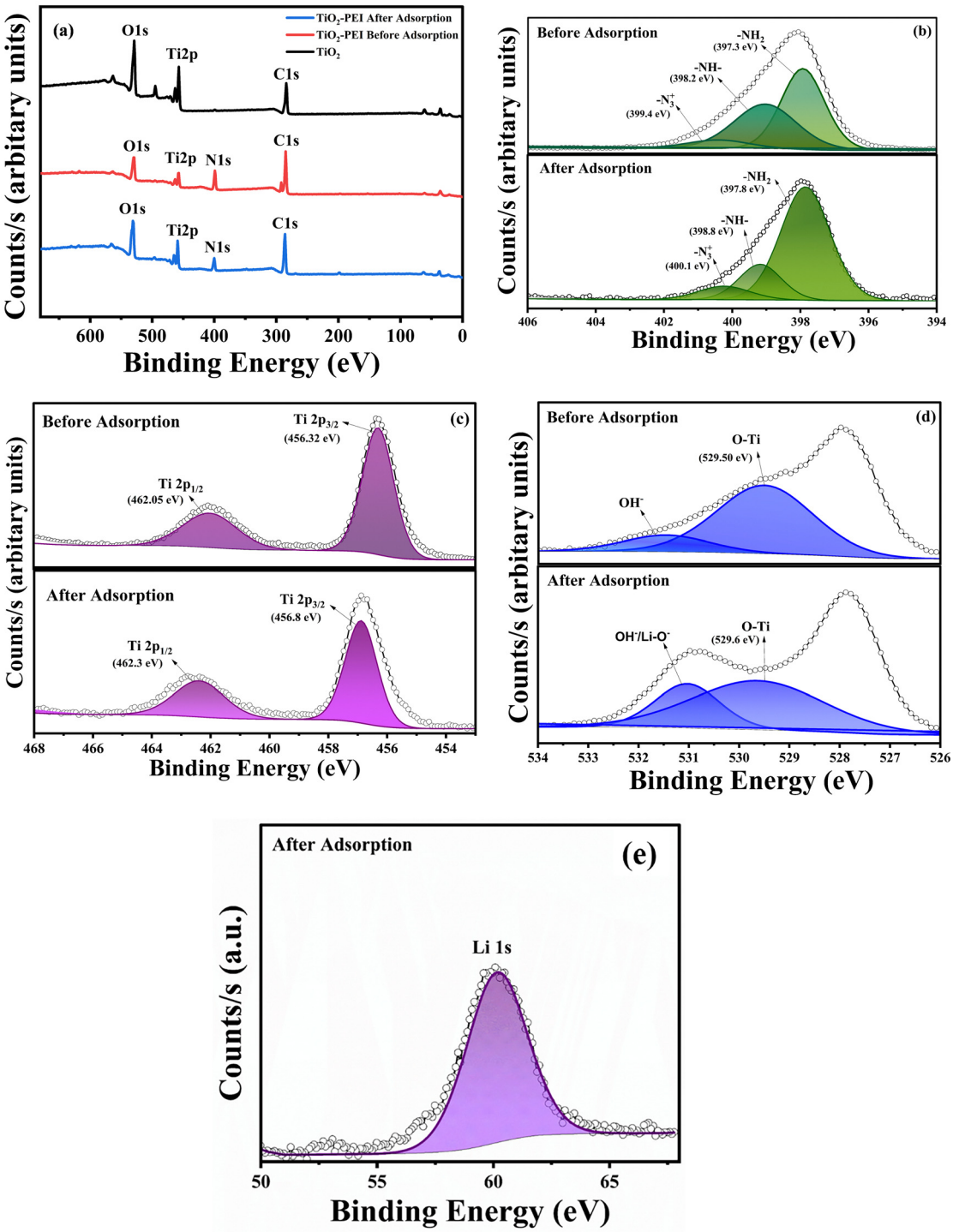

Fig. 6 X-ray photoelectron spectrum, (a) survey spectra, (b) deconvoluted N 1s spectra, (c) deconvoluted Ti 2p spectra, (d) deconvoluted O 1s spectra and (e) Li 1s spectra.

397.3 eV, 398.2 eV, and 399.4 eV[43,44] to 397.8 eV, 398.8 eV, and 400.1 eV, respectively, was observed. This can be attributed to the electrostatic interaction of the lithium-ion with the nitrogen atom that tends to provide electron density to the metal cation during its interaction, thereby reducing the electron density on the nitrogen atom. The core electrons are strongly pulled by the nucleus, which increases the binding energy.[45] Fig. 6c shows the deconvoluted spectra of Ti 2p; the binding energy of Ti $2p_{3/2}$ and Ti $2p_{1/2}$ increased after adsorption from 456.32 eV and 462.05 eV to 456.8 eV and 462.3 eV owing to the interaction of Li–O–Ti from O–Ti as can be observed from the deconvoluted oxygen spectra (Fig. 6d). The intensity of the peak decreased after adsorption likely due to the changes in the electronic environment of oxygen and lithium. Owing to the small size and polarizability, lithium interacts with the nearby electron cloud to a greater extent thereby reducing the electron density around the atom, thus increasing the binding energy.[46] There was no distinct change in the binding energies of C 1s[47,48] before and after adsorption, indicating a minimal to no direct interaction with lithium. Lithium was also detected in XPS at 60.2 eV, which confirms its presence on the adsorbent after adsorption (Fig. 6e).

3.1.6. Gas sorption analysis and DLS studies of the adsorbent. The BET-N_2 isotherm, or gas sorption analysis, provides insights into the adsorbent's surface characteristics, including specific surface area, pore diameter, and pore volume. Physical adsorption of liquid N_2 (77 K) onto the surface of the adsorbent provides the basis for the analysis. Fig. 7a illustrates the N_2 adsorption–desorption isotherm of the prepared adsorbent. The adsorbent was classified to be mesoporous, with a pore diameter of 40.59 nm (Fig. 7b) and a specific surface area of 45.3 $m^2\ g^{-1}$. The material exhibits a type-IV curve owing to its mesoporous nature, with the very slight hysteresis confirming the monolayer adsorption of molecules. When titanium nanorods with mesoporous nature (4.32 nm) were used for lithium adsorption, the efficiency was only 39%, attributed to the adsorbent's porous morphology, signifying the physisorption. However, after modifying the TiO_2(NR) with PEI, there was an increase in the pore size of the adsorbent and an increase in adsorption efficiency to 91%; this can be attributed to the interaction of TiO_2(NR) with PEI through electrostatic interactions that increase the available sites for lithium ions to interact through the ion exchange process, electrostatic attractions, and intermolecular hydrogen bonding. Therefore, the synergistic effect of the physicochemical interaction of the TiO_2(NR)–PEI with lithium ion aids in the removal with enhanced efficiency. The dynamic light scattering (DLS) technique was used to measure the particle size of the TiO_2-NRs before and after modification with PEI, Fig. S3(a–d) (ESI†). For DLS analysis, 0.1 mg of the TiO_2-NRs and TiO_2(NRs)–PEI was dispersed separately in 10 mL of DI water and sonicated for 15 min to achieve uniform material dispersion. A 5 μL of the above dispersion was added to 5 mL of DI water, and the particle size was measured. The hydrodynamic size of the particle, as given by the distribution curve, was 540 nm;[49,50] upon modification with the polymer, the particle's hydrodynamic size increased to 925 nm, affirming the addition of PEI to the nanorods.

3.2. Experimental variables

3.2.1. Effect of adsorbent dosage. To determine the optimal adsorbent dosage for achieving the maximum adsorption capacity, adsorbent dosage studies were carried out by varying the adsorbent dosage from 0.01 g to 0.15 g. The adsorption process was done using 10 mL of 10 mg L^{-1} lithium solution. It was observed (Fig. 8) that as the dosage of the adsorbent increases, the percentage of adsorption also increases linearly. This can be attributed to the availability of more active adsorption sites and functional groups for lithium to interact with the material efficiently, leading to the increased adsorption percentage. However, as the dosage exceeds 0.15 g, the adsorption percentage reaches saturation, indicating the optimal dosage for lithium adsorption. At higher adsorbent dosages, particle agglomeration can occur, which reduces the number of accessible active sites for lithium adsorption.[51]

3.2.2. Effect of pH on adsorption of lithium and the ZPC study. pH is a crucial factor that can significantly impact metal ion adsorption.[52] Studies were carried out by preparing lithium solutions at a fixed concentration, dosage, and volume in a pH range from 1.0 to 12.0, and adsorption was carried out for

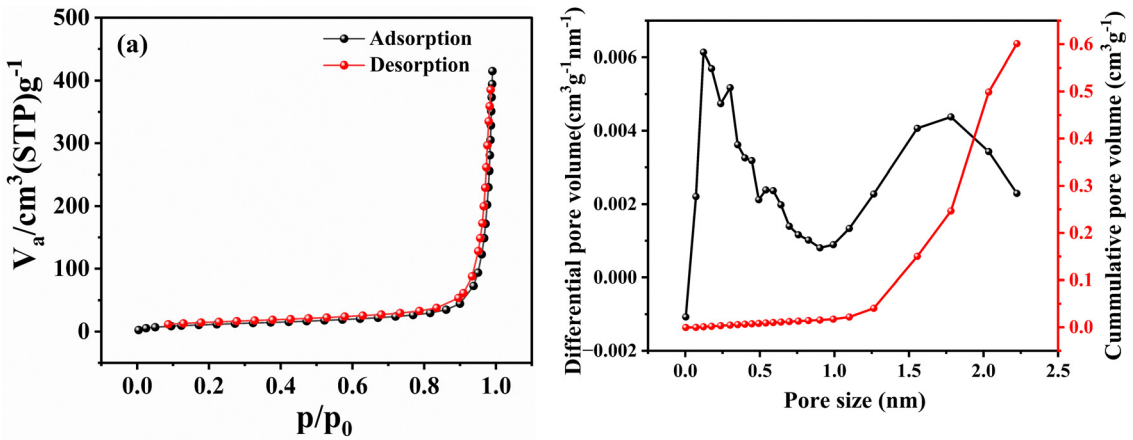

Fig. 7 (a) N_2 adsorption–desorption isotherm and (b) BJH plot of the adsorbent.

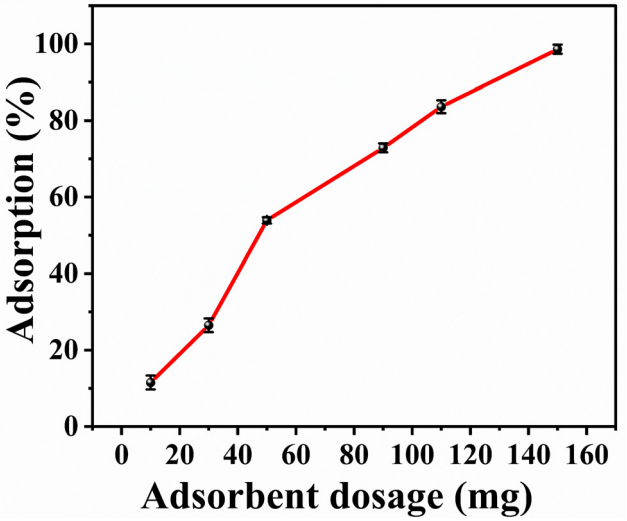

Fig. 8 Adsorbent dosage study by varying the TiO_2(NR)PEI dosage from 10 to 150 mg.

180 min on a vortex shaker to optimize the pH for maximum adsorption. As shown in Fig. 9, it was observed that as the pH increases, the adsorption percentage increases due to the highly electropositive nature of lithium, which relates to the electrostatic interaction with the surface negative charge developed at alkaline pH. At a lower pH, there would be a higher concentration of H^+ ions. The competition between the H^+ ions and the metal cation for interaction with the functional groups of the adsorbent may hinder the uptake of lithium. Since the surface would be positively charged the metal cation would be repelled by the surface of the adsorbent, resulting in a lower adsorption percentage at acidic pH. The zero-point charge (ZPC) of the adsorbent was determined using the pH drift method.[53] A 30 mL volume of 0.1 M NaOH was transferred to several conical flasks and the pH was varied from 1.0 to 12.0. To each flask, 100 mg of the adsorbent was added and kept in an incubator shaker at 100 rpm for 24 hours. After equilibration, the solutions were filtered, and their pH was recorded. The difference between initial and final pH was calculated and plotted against the pH as shown in Fig. 9b. It is evident that the isoelectric point for the adsorbent is 10.2. As pH increases above the ZPC, the surface of the adsorbent undergoes deprotonation and gains a negative charge. Conversely, below this point, there is an increase in H^+ ions leading to the protonation of the adsorbent surface.[54] This explains why the adsorption percentage increases at a higher pH.

3.3. Adsorption isotherm

Isotherm studies were conducted to gain a mechanistic understanding of the adsorptive recovery of lithium using TiO_2(NR)–PEI. According to the Langmuir isotherm, adsorption occurs on a homogeneous surface where the active sites are identical, and the rates of adsorption and desorption are considered to be equivalent, with all molecules having a constant enthalpy, identical activation energy, and equal affinity towards the surface of the material. The Freundlich model indicates the heterogeneous nature of the adsorbent and assumes that adsorption is a reversible process. This model also illustrates that at varying concentrations of the adsorbate, the ratio of the adsorbed species onto a certain mass of the adsorbent is not constant.[55] To perform isotherm studies, adsorption was carried out by varying the initial concentration of lithium solution from 10 mg L^{-1} to 100 mg L^{-1} with 0.15 g of the adsorbent throughout 3 h at 100 rpm in a vortex shaker. The experimental results were calculated and fitted with three different isotherm models: Langmuir, Freundlich, and Temkin, as illustrated in Fig. 10. The linear equation of the Langmuir model is expressed as,[56,57]

$$\frac{C_e}{q_e} = \frac{1}{q_{max}} C_e + \frac{1}{K_L q_{max}} \quad (2)$$

Here, C_e is the equilibrium concentration (mg L^{-1}), q_e is the equilibrium adsorption capacity (mg g^{-1}), q_{max} is the maximum adsorption capacity (mg g^{-1}), and K_L is the Langmuir constant (L mg^{-1}). From the linear Langmuir plot obtained by plotting

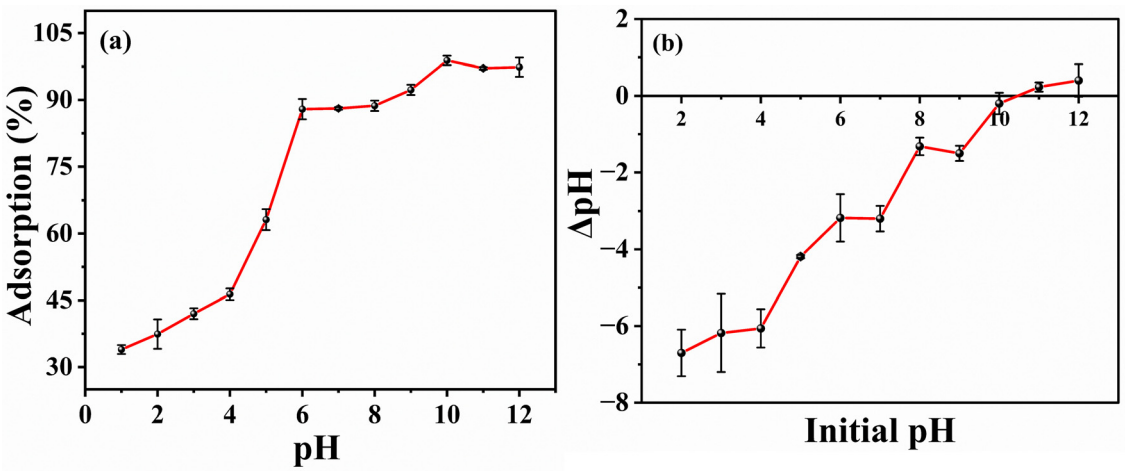

Fig. 9 (a) Effect of pH on adsorptive recovery of Li using TiO_2(NR)PEI and (b) zero-point charge (ZPC) determination for TiO_2(NR)PEI.

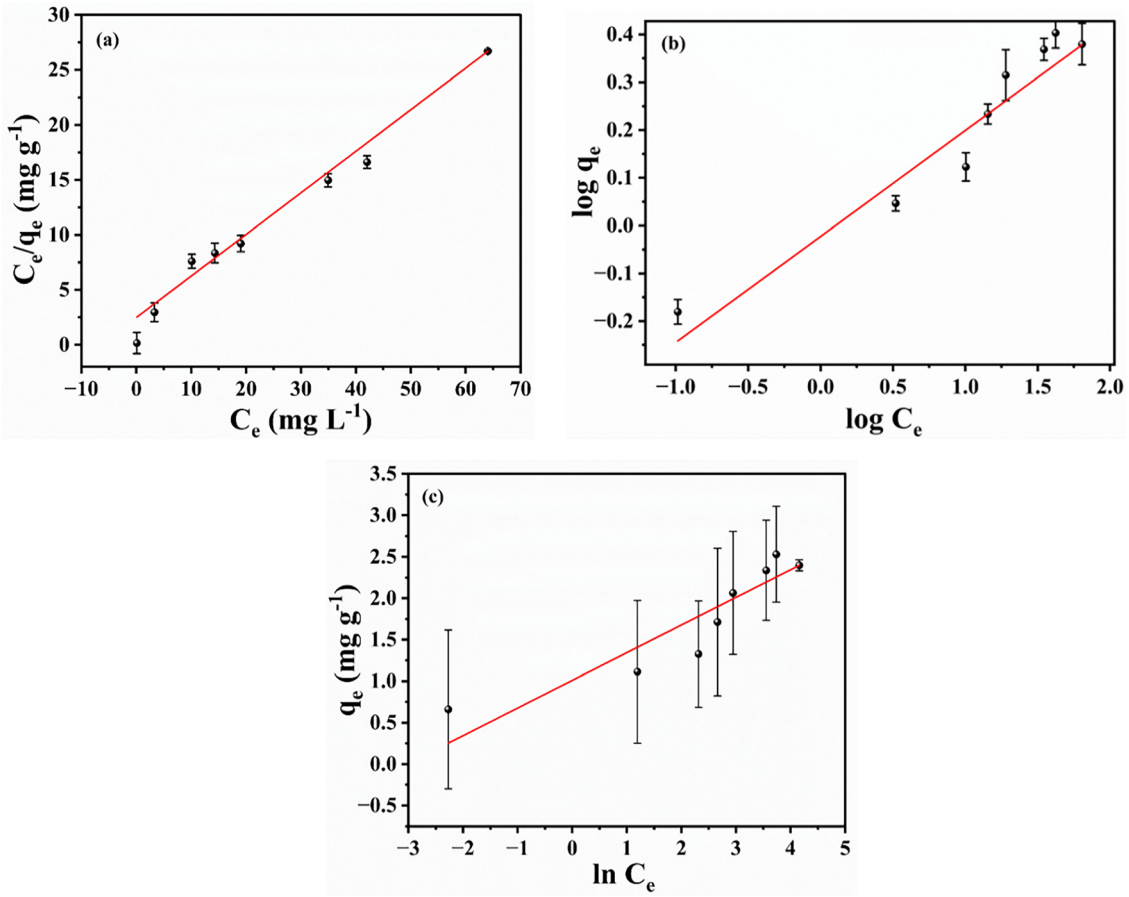

Fig. 10 (a) Langmuir linear isotherm plot, (b) Freundlich linear isotherm plot, and (c) Temkin linear isotherm plot.

$\frac{C_e}{q_e}$ *vs.* C_e the slope is $\frac{1}{q_{max}}$. The experimental results were fitted with the linear form of the Langmuir equation to obtain the maximum adsorption capacity of 2.76 mg g^{-1}. The linear equation for the Freundlich isotherm is given by,[58]

$$\log q_e = \log K_F + \frac{1}{n}\log C_e \quad (3)$$

where q_e is the equilibrium adsorption capacity (mg g^{-1}) of lithium, C_e is the initial concentration (mg L^{-1}), K_F is the adsorption capacity (mg$^{1-1/n}$ g^{-1} L$^{1/n}$), n is the constant obtained by plotting the experimental data in the linear Freundlich plot, $\log q_e$ *vs.* $\log C_e$, where K_F is the intercept and $1/n$ is the slope of the line, the calculated n value between 1 and 10 shows that the adsorption process is feasible.[17] Dimensionless constant R_L, also known as the separation factor, given by eqn (4), indicates the nature of adsorption $R_L = 1$, linear; $R_L = 0$, irreversible; $R_L > 1$, unfavourable and $0 < R_L < 1$, favorable.[59] The calculated R_L value for the concentration of 10 mg L^{-1} was 0.3, indicating a favourable reaction.

$$R_L = \frac{1}{1 + C_o K_L} \quad (4)$$

The Temkin isotherm considers the intermediate concentrations and eliminates lower and higher concentration values; according to this model, ΔH_{ads} of the adsorbate molecules on the surface reduces linearly as the surface coverage of the adsorbent increases. The following equation represents the linear form of the Temkin isotherm,[60]

$$q_e = \frac{RT}{b_{Te}} \ln K_T + \frac{RT}{b_{Te}} \ln C_e \quad (5)$$

Here, b_{Te} is the Temkin constant, representing the heat of adsorption in J mol^{-1}, K_T is the Temkin isotherm constant in L g^{-1}, R is the gas constant 8.314 J mol^{-1} K^{-1}, and T is the temperature in Kelvin. In this model, a plot of q_e *vs.* $\ln C_e$ is done from which the slope RT/b_{Te} and the intercept $RT/b_{Te} \ln K_T$ can be obtained. A higher correlation coefficient (R^2 = 0.998) from the fitted isotherm plots for the Langmuir isotherm, as in Table S1 (ESI†), shows that the adsorbent follows Langmuir adsorption, indicating that the adsorbent has homogeneous adsorption sites and matches with monolayer adsorption.

3.4. Adsorption kinetics

The kinetics study provides insight into the reaction rate concerning the adsorbate concentration and its interaction with the adsorbent.[61] A fixed concentration of lithium solution (10 mg L^{-1}), along with consistent adsorbent dosage and volume, was used to perform the kinetic studies. It was observed that equilibrium was attained in 180 min. Data obtained were fitted

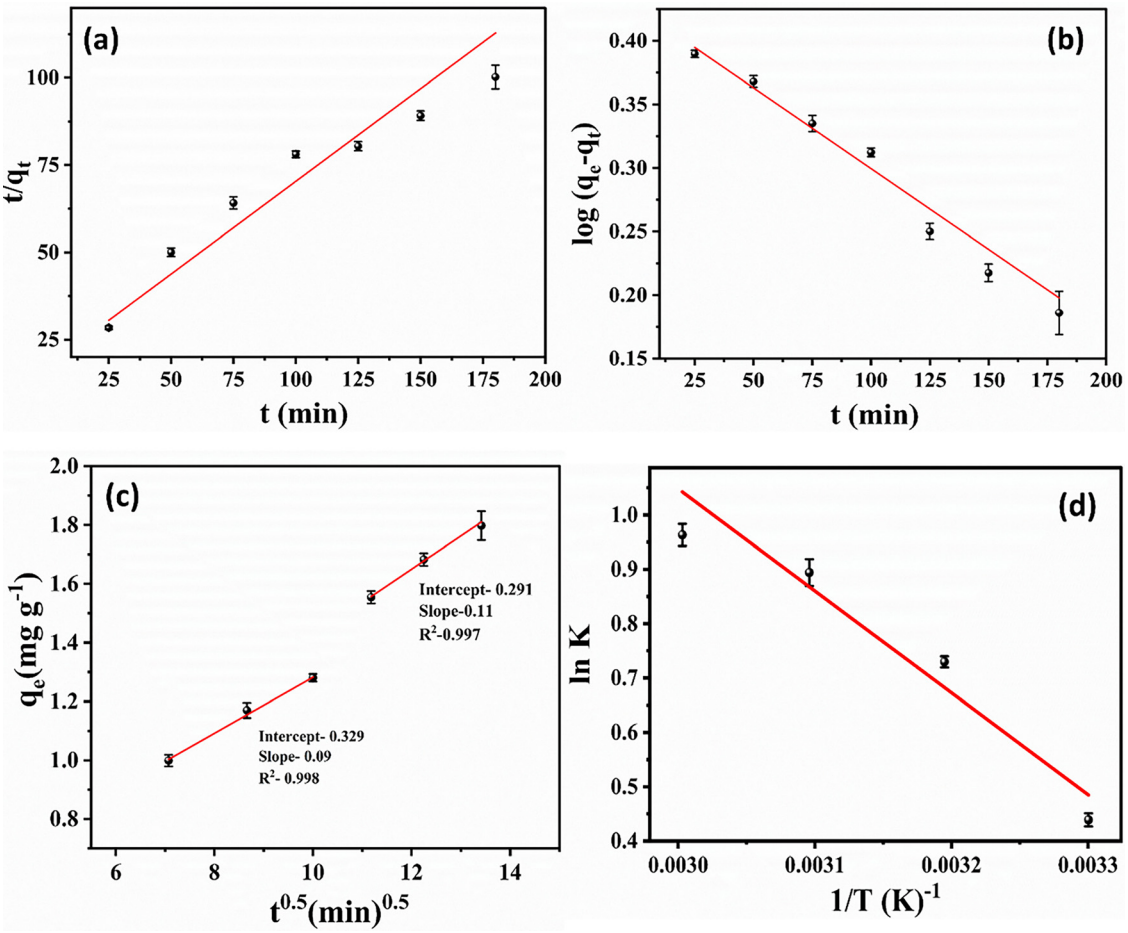

Fig. 11 (a) Pseudo-second-order kinetic model, (b) pseudo-first-order kinetic model, (c) intra-particle diffusion model and (d) thermodynamic study.

into two models, pseudo-first order and pseudo-second order (Fig. 11a and b).[62] Furthermore, the intraparticle diffusion model from the Weber–Morris plot as illustrated in Fig. 11c, was also considered to comprehend the uptake of lithium. The equations for the above models, respectively, are as follows:[63]

$$\log(q_e - q_t) = \log q_e - \left(\frac{k_1}{2.303}\right)t \quad (6)$$

$$\frac{t}{q_t} = \frac{t}{q_e} + \frac{1}{k_2 q_e^2} \quad (7)$$

where k_1 (min^{-1}) and k_2 (g mg^{-1} min^{-1}) are rate constants of pseudo-first and pseudo-second-order kinetics and q_e (mg g^{-1}) and q_t (mg g^{-1}) are equilibrium adsorption and adsorption capacity at time t (min). The pseudo-second-order model is a plot between, t *vs.* $\frac{t}{q_t}$, and pseudo-first-order between t *vs.* $\log(q_e - q_t)$. Initially, lithium adsorption occurs rapidly and continues to increase over time until it reaches equilibrium. This can be due to the positively charged lithium's electrostatic interaction with the adsorbent's negative surface. While comparing the R^2 value (correlation coefficient) from Table S2 (ESI†), it is evident that the pseudo-first-order model fitted the data with a higher R^2 value and the experimental and theoretically calculated q_e and q_t values, respectively, were also observed to be close. Thus, lithium's physico–chemical adsorption on the adsorbent's surface follows pseudo-first-order kinetics.[64]

$$q_t = t^2 K_i + C \quad (8)$$

where K_i is the intra-particle diffusion rate constant (mg g^{-1} $min^{-1/2}$) and C is the intercept that provides information about the thickness of the boundary.

Two stages of linearity indicate that the reaction proceeds through two steps. The first stage involves lithium diffusion from its bulk phase to the boundary layer through mass transfer, followed by diffusion onto the adsorbent, intraparticle diffusion. The second step is lithium binding *via* electrostatic interactions with surface functional groups of the adsorbent. It is evident from the slope of the two stages that both mass transfer and intraparticle diffusion are effective during adsorption.[65] Due to the atom's smaller size and the adsorbent's mesoporous nature, lithium would enter the pores of the adsorbent.[66]

3.5. Thermodynamic study

The thermodynamic nature and spontaneity of the process were evaluated by studying the effect of temperature on the

adsorption process, from which ΔG° (kJ mol^{-1}), ΔH° (kJ mol^{-1}), and ΔS° (kJ mol^{-1} K^{-1}) parameters were calculated from a linear Van't Hoff plot.[67] To perform this experiment, 50 mg L^{-1} of 10 mL lithium solution and 0.15 g of the adsorbent were taken in a centrifuge tube and placed on a vortex shaker at 700 rpm for 3 h at different temperatures (298 K, 308 K, 318 K, and 328 K), and the equilibrium concentration of lithium was analyzed.

$$\ln K_{eq} = \frac{-\Delta H^\circ}{R}\left(\frac{1}{T}\right) + \frac{-\Delta S^\circ}{R} \quad (9)$$

$$\Delta G^\circ = -RT \ln K_{eq} \quad (10)$$

K_{eq} is the equilibrium constant of the ratio of lithium ions on the adsorbent surface to those in the solution phase. The ΔH° (kJ mol^{-1}) and ΔS° (kJ mol^{-1} K^{-1}) were calculated from the slope and intercept of the plot $\ln K_{eq}$ *vs.* $\frac{1}{T}$. As illustrated in Fig. 11d, the adsorption capacity increases with an increase in temperature, affirming that the adsorption process is endothermic. Temperature is a driving factor[68] favouring increased activation energy for the diffusion of molecules into the bulk phase, as seen from the intraparticle diffusion model. The negative value obtained for ΔG° from the adsorbent at different temperatures indicates that the adsorption process is spontaneous, as detailed in Table S3 (ESI†). Additionally, the minimum and positive value of the change in entropy reflects the least randomness in the adsorbent–adsorbate interface.

3.6. Desorption and regeneration studies of the adsorbent

Regeneration and reusability are critical aspects of the practical applications of adsorbents.[69] To evaluate the reusability of TiO_2(NR)–PEI, desorption was conducted using 2.0 M H_3PO_4 over four successive adsorption–desorption cycles, as illustrated in Fig. 12. It was observed that after three continuous cycles, the adsorption percentage declined. As previously mentioned, the surface of the adsorbent also exhibits ion exchange properties. An increase in the concentration of H^+ ions effectively protonates the surface of the adsorbent, leading to a reversible adsorption–desorption process wherein they replace the Li^+ ions present on the surface of the adsorbent as their concentration increases. Desorption was then performed for 180 min. The supernatant was filtered and tested for lithium presence using UV-vis spectrophotometry. Thorin was employed as a complexing agent for lithium (ESI† provides the detailed procedure). The desorption efficiency for the first cycle was found to be 81%. This process was repeated for three successive cycles, after which the adsorption efficiency declined. This decrease may be attributed to the use of phosphoric acid for desorption, which could have altered the adsorbent's surface, as indicated by the changes observed in the SEM image (Fig. 3).

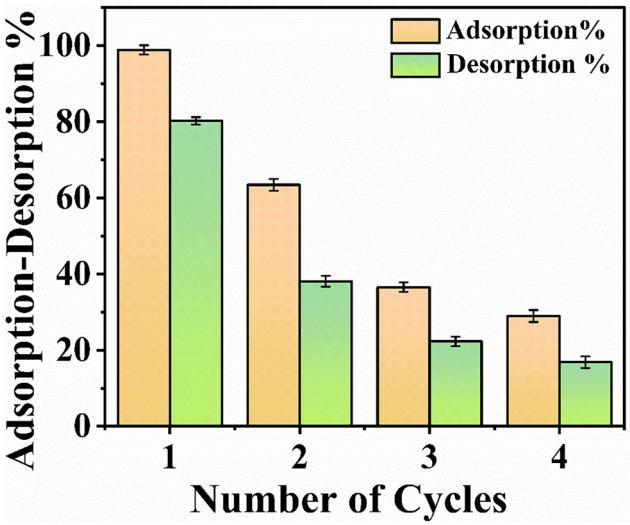

Fig. 12 Adsorption–desorption cycles of the synthesized adsorbent.

3.7. Mechanism of adsorption

3.7.1. Formation of TiO_2-NRs. The formation of nanorods occurs through the dissolution of titanium dioxide nanoparticles in a highly concentrated alkali solution, as given below[70]

$$TiO_2 + 2NaOH \rightarrow 2Na^+ + TiO_3^- + H_2O \quad (11)$$

Sodium titanate is formed as a soluble intermediate in the alkaline solution. When placed in an autoclave at elevated temperature, sodium titanate is dissolved and is re-precipitated, forming $Ti(OH)_4$. The highly alkaline environment leads the titanium oxide to grow in a particular direction, resulting in the formation of nanorods. The length and width of these nanorods can further be modified by altering the concentration of the base, temperature, and reaction time, which will bring about changes in the nucleation process; thus, the conditions can be tuned to achieve the desired morphology.[70]

3.7.2. Grafting of polyethyleneimine on TiO_2-NRs. PEI is dissolved in a suitable solvent to ensure uniform dispersion, essential for effective polymer coating onto the surface of titanium nanorods (Fig. 13a). Ethanol was used as a solvent, and its concentration was adjusted based on the required degree of functionalization. The primary interaction of the polymer with the surface of metal oxide occurs through electrostatic interaction between the positively charged amine and negatively charged titanium oxide surfaces, as PEI tends to protonate when dissolved in ethanol. The amine groups can also form chelation or coordinate bonds with the metal atom on the surface, creating a polymeric network around the nanorods and thereby improving their stability.

3.7.3. Adsorption of lithium. Polyethyleneimine has primary, secondary, and tertiary amine functionalities (–NH_2, –NH, and NH_3^+) and interacts with the positively charged lithium ion. Titanium dioxide nanorods develop a negative charge on the surface in a basic environment due to the deprotonation of hydroxyl groups and thus interact with lithium ions through

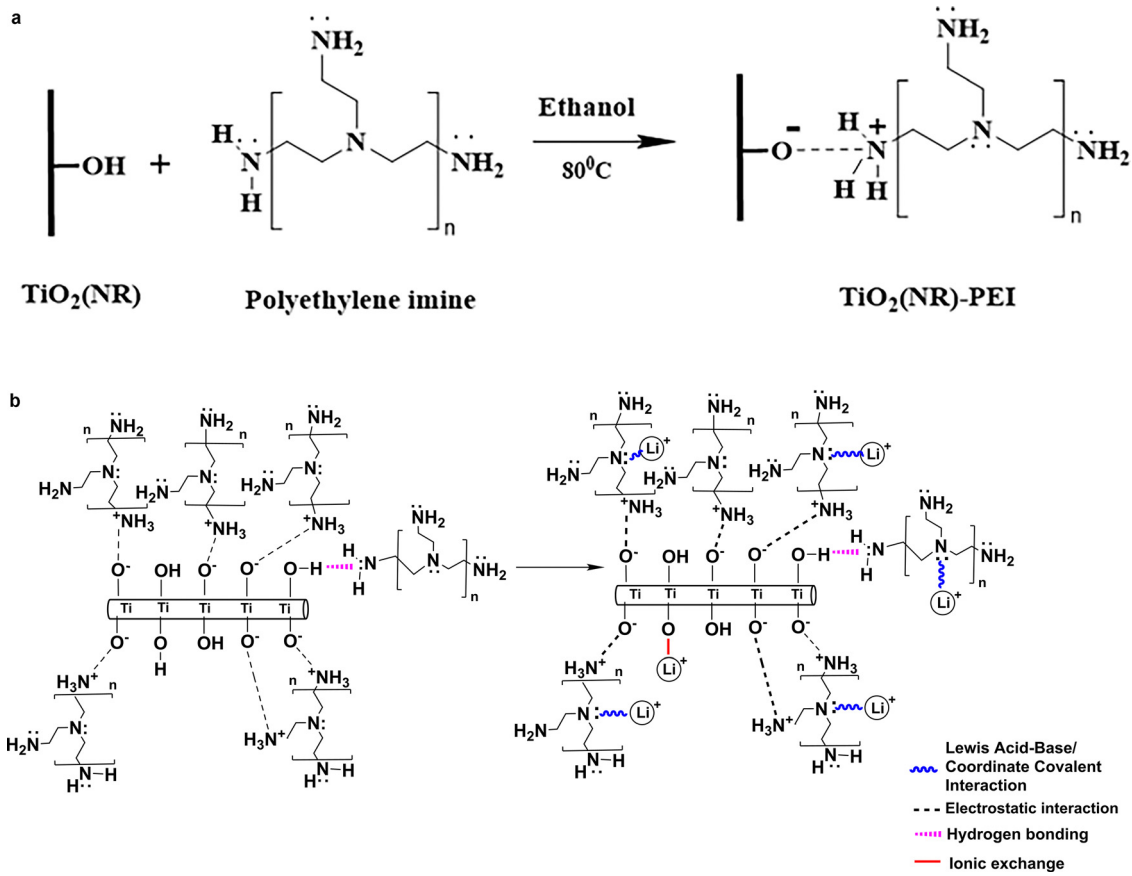

Fig. 13 (a) Interaction of titanium nanorods with polyethyleneimine. (b) Mechanistic view of the adsorption process.

electrostatic interaction. The lone pair on nitrogen atoms of the polymer can coordinate with lithium, owing to its electrophilic nature, therefore enhancing the adsorption. Lithium ions were stabilized electrostatically.[71] The amine groups of the polymer create a stable interface between the metal ion and the composite surface. Additionally, there can also be an ion exchange mechanism where the hydrogen is replaced with lithium on the surface of the titanium nanorods,[32]

$$TiO^{-} + Li^{+} \rightarrow TiO\text{–}Li \quad (12)$$

$$TiOH_2^{+} + Li^{+} \rightarrow TiO^{+}HLi + H^{+} \quad (13)$$

Owing to its mesoporous nature, lithium can also diffuse into the pores of the composite material, as supported by the kinetics and intra-particle diffusion model, which suggests that the adsorption takes place to some extent through this process. Thus, a synergistic influence of the above factors (Fig. 13b) is responsible for lithium adsorption onto the composite material's surface.

3.8. Lithium recovery from a battery cathode and brine solution

Recovery of metals from spent lithium-ion batteries has become an important aspect, and with the increasing demand for lithium globally, exploring and utilizing every feasible resource is of great value. The most conventional methods explored for recycling include pyrometallurgy and hydrometallurgy,[63–65] which have significant disadvantages that include the generation of tonnes of waste material, burning off the organic electrolyte that results in the loss of various valuable materials, emission of toxic gases, *etc.*, which would negatively impact the environment. Hence, more viable and energy-efficient techniques like adsorption have been employed to recover lithium. Here in this study, the developed adsorbent was tested for adsorption using commercially available $LiCoO_2$, the most commonly employed cathode material in lithium-ion batteries; 0.14 g of $LiCoO_2$ was taken and dissolved in a minimal amount of concentrated hydrochloric acid and evaporated until a blue precipitate was obtained, which was diluted with DI water and made up to 100 mL (100 ppm). The solution was further diluted to 10 ppm and used for performing adsorption and concentrated HCl was used to solubilize $LiCoO_2$. The adsorption and desorption were ascertained spectrophotometrically (Fig. 14). The adsorption percentage was found to be 69%, after which desorption was performed with 2.0 M H_3PO_4, and the desorption percentage was found to be 85%. A brine solution was prepared by dissolving 40 g of NaCl (15 480 ppm of Na^{+}) and 6.1 g of LiCl (1000 ppm of Li^{+}) in 1 L of water. The mixture was sonicated for 10 min and diluted to 10 ppm, after which adsorption was performed and analyzed spectrophotmetrically. The adsorption

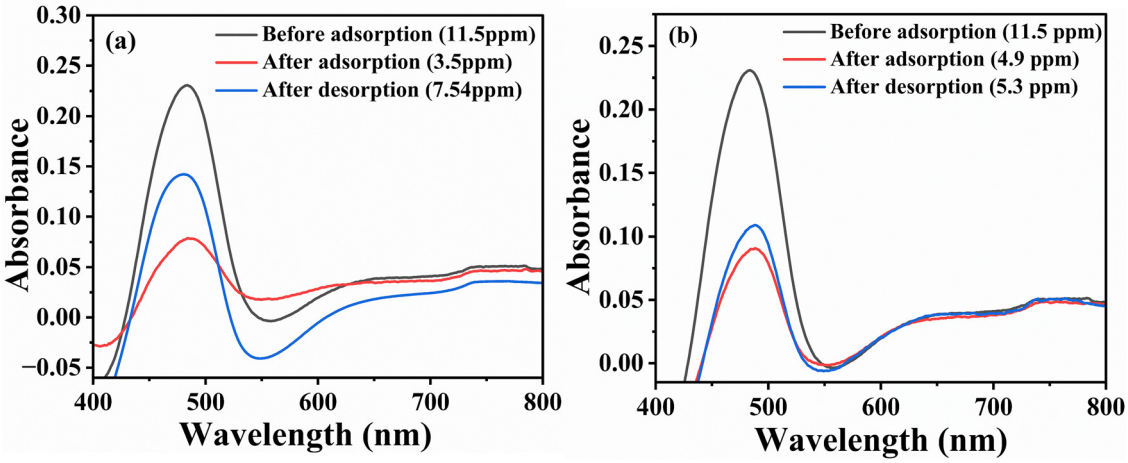

Fig. 14 (a) $LiCoO_2$ before, after adsorption, and desorption and (b) saline water before, after adsorption, and desorption.

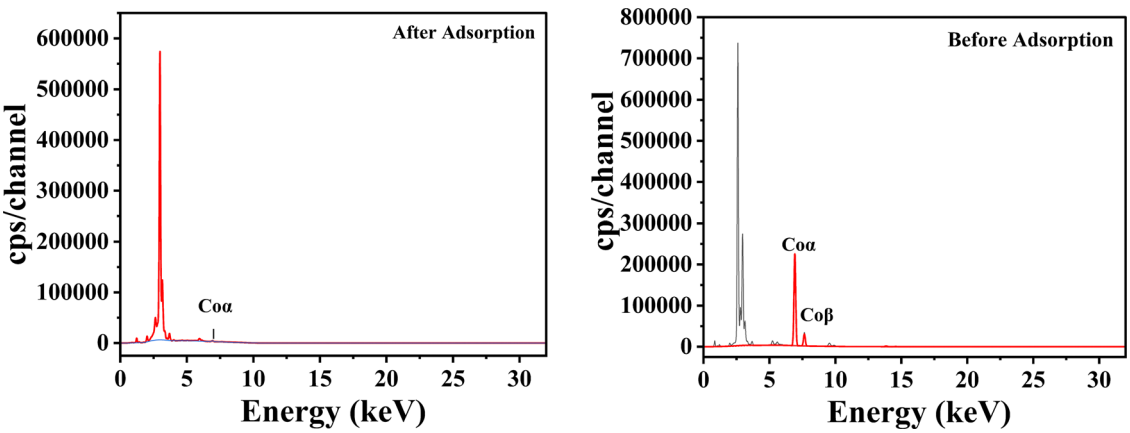

Fig. 15 X-ray fluorescence spectrum of before and after adsorption of lithium.

percentage was found to be 57%, and desorption was performed using 2.0 M H_3PO_4, which was found to be 84%. The decrease in adsorption capacity can be attributed to increased competition for the adsorption sites among the Li^+, Na^+, and Co^{2+} ions. It is evident from the XRF, as shown in Fig. 15, that the percentage of cobalt decreased after adsorption from 12.986% to 0.035%. The desorbed lithium phosphate was converted to its carbonate form and the pH of the desorbed solution was adjusted with 2.0 M NaOH until alkaline pH was obtained. Sodium carbonate was then added to the solution under constant stirring. It was kept on the hot plate at 50 °C overnight until lithium carbonate precipitated out, as it is sparingly soluble in water owing to its low K_{sp} value. The white precipitate was collected and calcined at 700 °C for 4 h to convert into lithium oxide and characterized. Fig. 16 presents the PXRD pattern of the calcinated sample and it is evident that peaks corresponding to lithium oxide are observed at 2θ values of 34.6 (101) and 58.6 (110) with unit cell parameters a = 3.1420 Å, b = 3.1420 Å, and c = 7.6500 Å (ref number: 01-074-0115) along with peaks relevant to sodium carbonate and sodium oxide as well.

Lithium oxide plays a crucial role in the production of cathode materials such as lithium cobalt oxide ($LiCoO_2$), lithium nickel manganese cobalt oxides (NMC), and lithium iron phosphate ($LiFePO_4$), which are needed to activate lithium-ion batteries in electric cars and portable electronics effectively. It is also being explored for developing solid-state electrolytes for lithium-ion batteries, which could potentially replace liquid electrolytes and improve performance and safety. Lithium oxide is also essential for lithium-air (Li-air) batteries, renowned for high energy density. Lithium oxide formation and breakdown during battery cycling are crucial to Li-air battery operation and provide the possibility of applications requiring long-lasting energy storage.[72] Lithium oxide is also an additive in glass and ceramics to augment their mechanical and thermal properties, including strength and melting point. So, recycling and lithium recovery will be vital to sustaining the supply of lithium oxide for the expanding energy and battery sectors.[73]

3.9. Selectivity studies

Adsorbent selectivity towards lithium was performed in the presence of Na^+, Mg^{2+}, and Co^{2+} respectively. The concentration was maintained at 10 ppm for each ion. The results (Fig. 17) showed that lithium adsorption is affected considerably and this

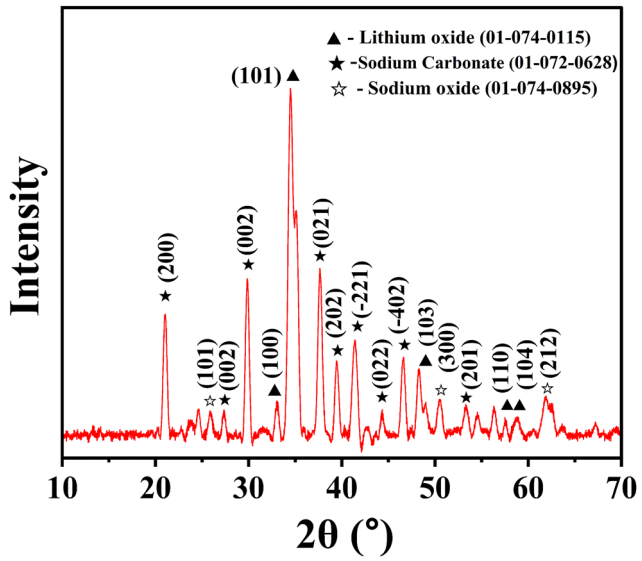

Fig. 16 PXRD pattern of recovered lithium oxide.

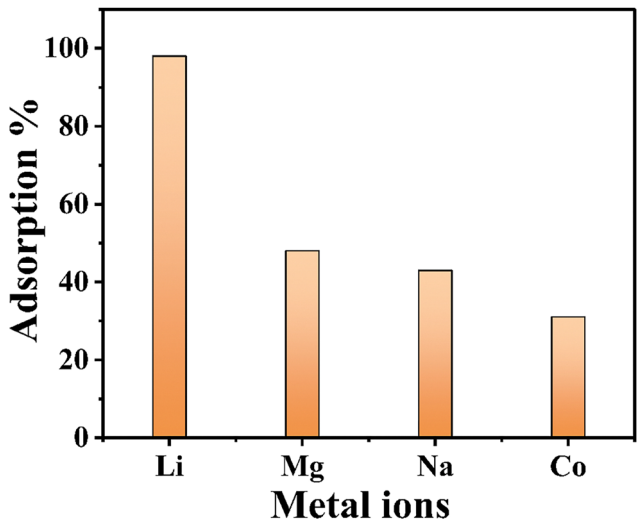

Fig. 17 Selectivity of lithium towards the adsorbent in the presence of Na^+, Mg^{2+}, and Co^{2+} ions.

is attributed to the fact that the charge density of the above metal ions being higher than that of lithium, they would also exhibit significant electrostatic interaction with the nitrogen and oxygen functionalities of the adsorbent. In our present application-oriented work, lithium adsorption was above 50% (52%, 59%, and 69%, respectively) for actual samples using the adsorbent TiO_2(NR)–PEI composite. The developed TiO_2-PEI adsorbent showed comparable adsorption capacity against a few related adsorbents previously reported in the literature (Table S4, ESI†).

4. Conclusion

Lithium adsorption was successfully achieved by the hydrothermally synthesized titanium nanorods and modified with polyethyleneimine through a wet impregnation method. The study investigated the uptake of Li^+ by this synthesized composite, revealing that the optimal conditions for maximum adsorption occurred at a pH of 10, with an adsorbent dosage of 0.15 g and an equilibrium contact time of 180 minutes. The zero potential charge (ZPC) confirmed these results, indicating an isoelectric point at 10.2. The kinetic model determined the mechanism of adsorption, where it was found that the pseudo-first-order model fitted the kinetics plot with the highest regression coefficient. Thermodynamic studies showed that the adsorption was endothermic. Maximum adsorption was 98%, and lithium adsorption capacity was calculated as 2.76 mg g^{-1}. The reusability of the composite material was verified from four repetitive adsorption/desorption cycles and it was found after the 4th cycle, the adsorption efficiency decreased. The material was also tested for the adsorption of Li^+ from commercial $LiCoO_2$ and a concentrated brine solution under the above-optimized conditions, wherein the adsorption was found to be 69% and 57%, respectively. Lithium desorbed as lithium phosphate was converted to lithium oxide, as supported by the XRD pattern. Hence, the results demonstrate that the TiO_2(NR)–PEI composite has good potential for lithium adsorption and recovery. The encouraging results have propelled us to modify metal oxides with more suitable functionalization to offer higher adsorption/recovery to be explored in our subsequent study.

Author contributions

N. Rajesh and Himanshu Aggarwal were involved in conceptualizing the work, and K. Krishna Priyanka and M. Christina Nilavu performed all the experiments related to adsorption. K. Krishna Priyanka was also involved in acquiring data for all analytical characterization methods. B. Arunraj was involved in studies and interpretations about analytical characterization methods and manuscript writing.

Data availability

The datasets generated during and/or analysed during the current study are not publicly available due to confidentiality of the results, but are available from the authors upon reasonable request.

Conflicts of interest

The authors declare no conflict of interest.

Acknowledgements

The authors acknowledge the Central Analytical Laboratory, BITS Pilani, Hyderabad Campus, India, for their support in the analytical characterization techniques.

References

1 T. Kanagasundaram, O. Murphy, M. N. Haji and J. J. Wilson, *Coord. Chem. Rev.*, 2024, **509**, 215727.
2 Z. J. Baum, R. E. Bird, X. Yu and J. Ma, *ACS Energy Lett.*, 2022, **7**, 712–719.
3 M. Chen, X. Ma, B. Chen, R. Arsenault, P. Karlson, N. Simon and Y. Wang, *Joule*, 2019, **3**, 2622–2646.
4 J. W. Fergus, *J. Power Sources*, 2010, **195**, 939–954.
5 A. Khor, P. Leung, M. R. Mohamed, C. Flox, Q. Xu, L. An, R. G. A. Wills, J. R. Morante and A. A. Shah, *Mater. Today Energy*, 2018, **8**, 80–108.
6 Peter E. Stokes, Peter M. Stoll, Charles A. Shamoian and Michael J. Patton, *Lancet*, 1971, 1319–1325.
7 W. Young, *Cell Transplant.*, 2009, **18**, 951–975.
8 V. Flexer, C. F. Baspineiro and C. I. Galli, *Sci. Total Environ*, 2018, **639**, 1188–1204.
9 L. H. Chan, W. P. Leeman and T. Plank, *Geochem., Geophys., Geosyst.*, 2006, **7**, Q06005.
10 R. Chitrakar, H. Kanoh, Y. Miyai and K. Ooi, *Ind. Eng. Chem. Res.*, 2001, **40**, 2054–2058.
11 Y. Miyai, K. Ooi and S. Katoh, *Sep. Sci. Technol.*, 1988, **1–3**, 179–191.
12 T. S. Volkova, V. V. Rudskikh, V. A. Orlova and I. G. Tananaev, *Russ. J. Appl. Chem.*, 2015, **88**, 1388–1394.
13 M. Rona and G. Schmuckler, *Talanta*, 1973, **20**, 237–240.
14 J. F. Song, L. D. Nghiem, X. M. Li and T. He, *Environ. Sci.: Water Res. Technol.*, 2017, **3**, 593–597.
15 Q. Yu, K. Sasaki and T. Hirajima, *J. Hazard. Mater.*, 2013, **262**, 38–47.
16 B. Swain, *Sep. Purif. Technol.*, 2017, **172**, 388–403.
17 Y. K. Recepoğlu, N. Kabay, İ. Yılmaz-Ipek, M. Arda, K. Yoshizuka, S. Nishihama and M. Yüksel, *Solvent Extr. Ion Exch.*, 2017, **35**, 221–231.
18 X. Wen, P. Ma, C. Zhu, Q. He and X. Deng, *Sep. Purif. Technol.*, 2006, **49**, 230–236.
19 M. Hartono, M. A. Astrayudha, H. T. B. M. Petrus, W. Budhijanto and H. Sulistyo, *Rasayan J. Chem.*, 2017, **10**, 897–903.
20 D. C. R. Espinosa, A. M. Bernardes and J. A. S. Tenório, *J. Power Sources*, 2004, **135**, 311–319.
21 X. Zeng, J. Li and L. Liu, *Renewable Sustainable Energy Rev.*, 2015, **52**, 1759–1767.
22 M. Zhou, J. Shen, Y. Zuo, R. Liu, J. Zhao and G. Zhou, *Angew. Chem., Int. Ed.*, 2024, e202414484.
23 Y. Miao, L. Liu, Y. Zhang, Q. Tan and J. Li, *J. Hazard. Mater.*, 2022, **425**, 127900.
24 M. Iturrondobeitia, C. Vallejo, M. Berroci, O. Akizu-Gardoki, R. Minguez and E. Lizundia, *ACS Sustainable Chem. Eng.*, 2022, **10**, 9798–9810.
25 Y. K. Recepoğlu and A. Yüksel, *Cellul. Chem. Technol.*, 2021, **55**, 385–401.
26 J. Chen, S. Lin and J. Yu, *J. Hazard. Mater.*, 2020, **388**, 122101.
27 J. Zhong, S. Lin and J. Yu, *J. Colloid Interface Sci.*, 2020, **572**, 107–113.
28 L. T. Menzheres, A. D. Ryabtsev and E. V. Mamylova, *Theor. Found. Chem. Eng.*, 2019, **53**, 821–826.
29 X. Xu, Y. Chen, P. Wan, K. Gasem, K. Wang, T. He, H. Adidharma and M. Fan, *Prog. Mater. Sci.*, 2016, **84**, 276–313.
30 X. C. Shi, Z. B. Zhang, D. F. Zhou, L. F. Zhang, B. Z. Chen and L. L. Yu, *Trans. Nonferrous Met. Soc. China*, 2013, **23**, 253–259.
31 S. Wang, P. Li, X. Zhang, S. Zheng and Y. Zhang, *Hydrometallurgy*, 2017, **174**, 21–28.
32 C. Thanh Nam, W. Yang and L. Minh Duc, *Bull. Mater. Sci.*, 2013, **36**, 779–788.
33 U. Kamran and S.-J. Park, *J. Solid State Chem.*, 2020, **283**, 121157.
34 R. Govindaraj, N. Santhosh, M. Senthil Pandian and P. Ramasamy, *Appl. Surf. Sci.*, 2018, **449**, 166–173.
35 N. B. Mohamed, N. Ngadi, S. Wong, N. Y. Yahya, O. Hassan, I. M. Inuwa, L. A. Opotu and N. Ali, *Sci. Afr.*, 2022, **16**, e01135.
36 W. Xu, J. Y. Park, K. Kattel, M. W. Ahmad, B. A. Bony, W. C. Heo, S. Jin, J. W. Park, Y. Chang, T. J. Kim, J. A. Park, J. Y. Do, K. S. Chae and G. H. Lee, *RSC Adv.*, 2012, **2**, 10907–10915.
37 T. Maiyalagan and B. Viswanathan, *Mater. Chem. Phys.*, 2005, **93**, 291–295.
38 X. A. Zhao, C. W. Ong, Y. C. Tsang, Y. W. Wong, P. W. Chan and C. L. Choy, *Appl. Phys. Lett.*, 1995, **66**, 3368.
39 P. Bindra, H. Mittal, B. R. Sarkar and A. Hazra, *J. Electron. Mater.*, 2022, **51**, 1707–1716.
40 L. Yesappa, M. Niranjana, S. Ashokkumar, H. Vijeth, S. Raghu and H. Devendrappa, *Polym.-Plast. Technol. Mater.*, 2019, **58**, 193–205.
41 B. Huang, Y. Liu, B. Li, H. Wang and G. Zeng, *RSC Adv.*, 2019, **9**, 32462–32471.
42 S. Kalaiarasi and M. Jose, *Appl. Phys. A: Mater. Sci. Process.*, 2017, **123**, 512.
43 C. Xing, C.-Y. Liu, C. Lai and S.-Q. Zhang, *Rare Met.*, 2023, **42**, 418–429.
44 W. C. Wu, H. Y. T. Chen, S. C. Lin, H. Y. Chen, F. R. Chen, H. T. Chang and F. G. Tseng, *Mikrochim, Acta*, 2019, **186**, 1–8.
45 J. Lan, B. Wang and B. Gong, *Water Sci. Technol.*, 2022, **86**, 2465–2481.
46 X. Luo, K. Zhang, J. Luo, S. Luo and J. Crittenden, *Environ. Sci. Technol.*, 2016, **50**, 13002–13012.
47 H. He, X. Hou, B. Ma, L. Zhuang, C. Li, S. He and S. Chen, *Cellulose*, 2016, **23**, 2539–2548.
48 Z. Mou, B. Wang and Z. Huang, *Fullerenes, Nanotubes Carbon Nanostruct.*, 2019, **27**, 899–906.
49 P. Bindra, H. Mittal, B. R. Sarkar and A. Hazra, *J. Electron. Mater.*, 2022, **51**, 1707–1716.
50 C. B. Tovani, C. R. Ferreira, A. M. S. Simão, M. Bolean, L. Coppeta, N. Rosato, M. Bottini, P. Ciancaglini and A. P. Ramos, *ACS Omega*, 2020, **5**, 16491–16501.
51 U. Kamran, H. N. Bhatti, M. Iqbal, S. Jamil and M. Zahid, *J. Mol. Struct.*, 2019, **1179**, 532–539.

52 S. Liang, S. Cao, C. Liu, S. Zeb, Y. Cui and G. Sun, *RSC Adv.*, 2020, **10**, 7259–7264.
53 M. Christina Nilavu, B. Arunraj, H. Aggarwal and N. Rajesh, *Fuel*, 2022, **324**, 124472.
54 H. Wu, L. Gong, X. Zhang, F. He and Z. Li, *Chem. Eng. J.*, 2021, **411**, 128539.
55 M. Christina Nilavu, B. Arunraj, H. Aggarwal and N. Rajesh, *Fuel*, 2023, **345**, 128172.
56 Y. Li, M. D. Chen, X. Wan, L. Zhang, X. Wang and H. Xiao, *RSC Adv.*, 2017, **7**, 53899–53906.
57 R. Karthik and S. Meenakshi, *Int. J. Biol. Macromol.*, 2014, **67**, 210–219.
58 H. Wu, W. Zhang, H. Zhang, Y. Pan, X. Yang, Z. Pan, X. Yu and D. Wang, *Colloids Surf., A*, 2020, **607**, 125517.
59 M. A. Al-Ghouti and D. A. Da'ana, *J. Hazard. Mater.*, 2020, **393**, 122383.
60 J. S. Piccin, G. L. Dotto and L. A. A. Pinto, *Braz. J. Chem. Eng.*, 2011, **28**, 295–304.
61 S. Sen Gupta and K. G. Bhattacharyya, *Adv. Colloid Interface Sci.*, 2011, **162**, 39–58.
62 S. Sedaghat, M. M. Ahadian, M. Jafarian and S. Hatamie, *Ind. Eng. Chem. Res.*, 2019, **58**, 10341–10351.
63 H. Qiu, L. Lv, B. C. Pan, Q. J. Zhang, W. M. Zhang and Q. X. Zhang, *J. Zhejiang Univ., Sci.*, 2009, **10**, 716–724.
64 B. Liu, H. Luo, H. Rong, X. Zeng, K. Wu, Z. Chen, H. Lu and D. Xu, *Desalin. Water Treat.*, 2019, **160**, 260–267.
65 M. Daneshvar and M. R. Hosseini, *Environ. Sci. Pollut. Res.*, 2018, **25**, 28654–28666.
66 P. S. Kumar and R. Gayathri, *J. Eng. Sci. Technol.*, 2009, **4**, 381–399.
67 D. Shao, Y. Li, X. Wang, S. Hu, J. Wen, J. Xiong, A. M. Asiri and H. M. Marwani, *ACS Omega*, 2017, **2**, 3267–3275.
68 M. M. Saeed and M. Ahmed, *Sep. Sci. Technol.*, 2006, **41**, 705–722.
69 S. Zhang, Q. Du, Y. Sun, J. Song, F. Yang and D. C. W. Tsang, *Sci. Total Environ*, 2020, **720**, 137415.
70 T. Gupta, Samriti, J. Cho and J. Prakash, *Mater. Today Chem.*, 2021, **20**, 100428.
71 T. Wang, M. Jiang, X. Yu, N. Niu and L. Chen, *Sep. Purif. Technol.*, 2022, **302**, 122116.
72 Y. Wang, W. D. Richards, S. P. Ong, L. J. Miara, J. C. Kim and G. Ceder, *Nat. Mater.*, 2015, **14**, 1026–1031.
73 N. Dechboon, A. Nuntiya, C. Saelee and S. Thiansem, *Key Eng. Mater.*, 2020, **858**, 146–150.